ACS OMEGA

Open Access

http://pubs.acs.org/journal/acsodf

Article

Reflectionless Linear Polarization Rotators with Angular Robustness

Hadi Ahmadi, Sanchita Sarker, and Mohammad Parvinnezhad Hokmabadi*

Cite This: *ACS Omega* 2026, 11, 6264−6274

Read Online

ACCESS | Metrics & More | Article Recommendations

ABSTRACT: An open challenge in integrated polarization optics is creating compact, alignment-free rotators that maintain low reflection at a constant thickness. This capability is essential for compatibility with scalable wafer-level fabrication. In this work, we numerically design a terahertz chiral bilayer metasurface that uses 4-fold rotational (C_4) symmetry to achieve prescribed linear-polarization rotations with near-zero reflection over a wide range of incident angles. The C_4 symmetry inherently removes cross-polarized reflection across the spectrum, while a destructive interference eliminates the copolarized reflectivity at a target resonance. A key novelty of our approach is that reflectionless response is maintained across diverse rotation angles without need to change the device thickness. Simulations further show that the structure remains reflectionless for incidence angles up to ∼20°, confirming strong angular robustness. Our design surpasses natural optical rotators, such as quartz, which require bulky thickness, and existing metasurfaces that rely on multilayer stacks or thickness variations to achieve reflectionless operation across varied rotation angles. The potential applications include integrated secure optical communications, parallel photonic processing, and advanced imaging systems.

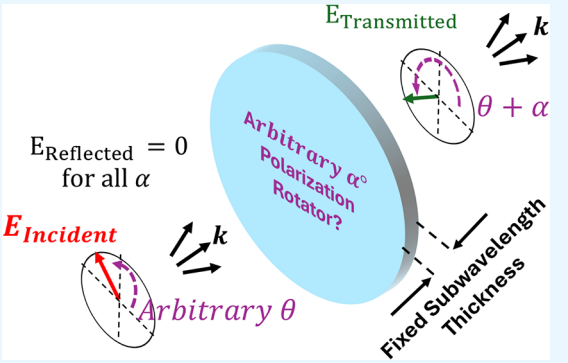

INTRODUCTION

While intensity and wavelength often dominate our perception of light, polarization is an equally fundamental property in optics and electromagnetism. It plays a critical role across diverse scientific and technological domains, including imaging, spectroscopy, communication, remote sensing, and quantum systems.[1−6] Historically, azimuthal-free polarization manipulation has relied on natural materials exhibiting optical activity, such as crystalline quartz, which rotates the plane of linearly polarized light via its internal chiral composition. However, these materials suffer from inherently weak chiral responses, requiring large physical thicknesses to achieve desirable rotation, especially at longer wavelengths such as in the microwave, terahertz, or mid-infrared bands.[7−9] Furthermore, natural optical rotators provide only a uniform bulk response and cannot enable compact devices capable of spatially varying or pixel-level polarization transformations on vector beams, functionalities that are increasingly critical for advanced applications such as polarimetric imaging, beam shaping, and heterogeneous photonic systems.[10−13]

Metasurfaces, planar arrays of engineered subwavelength scatterers, have emerged as a powerful alternative, offering compact polarization control and flexible design freedom. Over the past two decades, they demonstrated promising results in manipulating polarization beyond natural materials, from early perfect polarization rotators for a known input state[14,15] to more recent advances in conversion efficiency,[16−18] degree of linearity,[19−21] bandwidth,[22−25] and geometric tunability through tailored unit cells and multilayer stacking.[26−32] In practical systems, however, input polarization is often unknown or varies unpredictably, making it essential to develop devices insensitive to incident polarizations and thus with high tolerance to misalignment. Although several metasurface-based approaches have verified such functionality,[33−45] achieving it in a compact, thickness-invariant, and transmissive form, while most importantly, maintaining near-zero reflectivity over a broad range of incidence angles, remains an open challenge. This difficulty becomes especially critical in chiral metasurfaces, since resonant subwavelength scatterers interact differently with each polarization component.[46,47] Consequently, they scatter light into both co- and cross-polarized channels, producing complex interference patterns that are highly sensitive to the input polarization. This sensitivity makes it intrinsically difficult to achieve impedance matching across all possible input states.

Recently, highly efficient devices capable of arbitrary polarization transformation have been reported, but they typically operate in reflection mode or use several multiple layers,[48,49] which limits their integration in many optical

Received: October 21, 2025
Revised: January 7, 2026
Accepted: January 12, 2026
Published: January 16, 2026

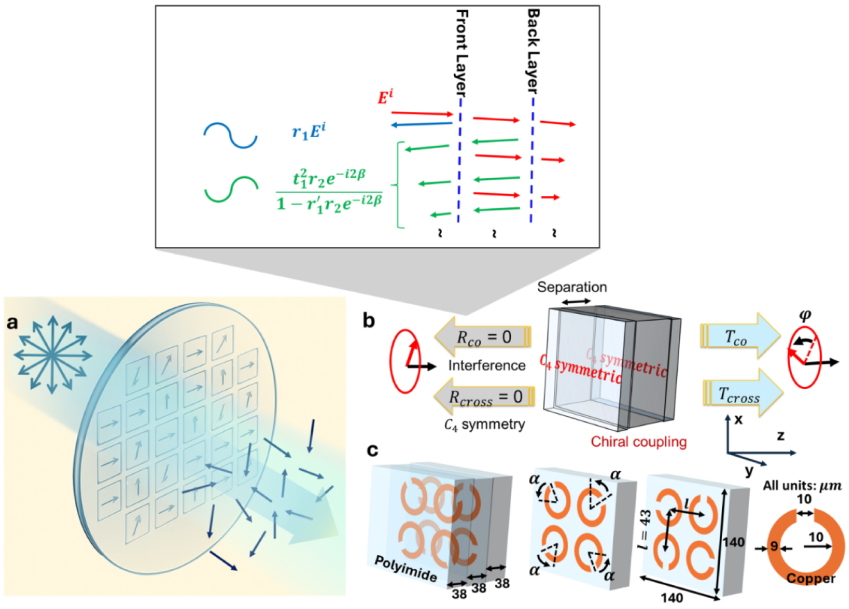

Figure 1. (a) Hypothetical demonstration of a device with reflectionless polarization manipulation capability across multiple rotators, all made on a single wafer with uniform thickness. (b) Conceptual illustration of the mechanism under which the reflectionless C_4-symmetric chiral setting performs. It rotates an incident wave of arbitrary polarization by an angle φ, at a constant device thickness. The C_4 symmetry suppresses cross-polarized reflection, while destructive interference between the two layers eliminates coreflectivity. The destructive interference arises between the field reflected directly from the front layer and the effective field resulting from multiple reflections between the two layers. In Figure (b), r_1 denotes the copolarized reflection coefficient of the front layer for incidence from the front side, while t_1 is the corresponding transmission coefficient through the same layer. The coefficient r_2 represents the copolarized reflection from the back layer as seen from the spacer. The phase factor β accounts for propagation through the spacer between the layers. The coefficient r_1' denotes the copolarized reflection coefficient of the front layer for incidence from the spacer (reverse side). (c) Schematic of the unit cell of our periodic structure to implement the concept of reflectionless polarization rotators. It is made of three layers. The identical split-ring resonators (SRRs) are made from copper (1 μm thick) on polyimide films, with the whole structure capped by an additional 38 μm polyimide layer. The twist angle α of SRRs in front layer primarily determines the polarization rotation angle φ, with zero reflectivity and without changing layer's thickness.

Table 1. Comparison of Findings from This Work with Those from Other Related Works

Article	Property A[a]	Property B[b]	Property C[c]	Property D[d]	Property E[e]	Property F[f]
This work	Yes	Yes	Yes	Yes	Yes	Yes
Ref. 14	Yes	No	No	No	No	No
Ref.15	Yes	No	No	Yes	No	No
Ref.18	Yes	No	No	No	No	No
Ref.21	No	No	No	No	No	No
Ref.29	Yes	No	No	No	No	No
Ref.44	Yes	No	No	No	No	Yes
Ref.48	No	No	No	No	No	No
Ref.47	No	No	No	No	Yes	No
Ref.52	Yes	No	No	No	Yes	Yes
Ref.55	Yes	No	No	No	Yes	No
Ref.56	No	No	Yes	Yes	No	No
Ref.57	No	No	Yes	Yes	No	No
Ref.58	Yes	No	No	No	No	No

[a]Property A: Transmissive and nondiffractive operation. [b]Property B: Reflection suppression across different rotations at fixed target frequency with a fixed thickness. [c]Property C: Angular robustness up to ~20° for TE and TM incidence. [d]Property D: Nonelliptical and linear polarization conversion at a fix target frequency (ellipticity < 0.6°). [e]Property E: Multiple rotation angles (45°, 60°, 90°, etc.) at a fixed target frequency. [f]Property F: Polarization-independent response.

systems. The challenge becomes even more pronounced in heterogeneous polarization platforms, where transformations must be performed locally, pixel by pixel or in parallel, while preserving a uniform device thickness compatible with planar wafer fabrication methods. A solution that simultaneously enables arbitrary input handling, and reflectionless polarization transformation within a transmissive, compact, and scalable platform has remained elusive.

Numerous prior studies have convincingly demonstrated polarization rotation using bilayer chiral metasurfaces, twisted multilayer configurations, and C_4-symmetric designs, including works that achieve large rotation angles, polarization-independent response, or tolerance to incidence angle for specific device geometries.[14−21,29,44,47,48,52,55−58] These contributions represent significant advances in polarization conversion efficiency and symmetry-based design strategies,

https://doi.org/10.1021/acsomega.5c11042
ACS Omega 2026, 11, 6264−6274

and they establish polarization rotation as a well-developed capability. However, in nearly all such implementations, reflection suppression is either not addressed or is optimized only for a specific twist angle (or polarization rotation/conversion) and spacer thickness at a target resonance frequency. When reflection minimization is considered, it typically relies on thickness-sensitive destructive interference at a target frequency, requiring reoptimization of the spacer thickness for each polarization rotation angle or ellipticity state.

This limitation becomes particularly problematic for applications requiring structured polarization conversion, where multiple polarization-rotation elements with different rotation angles must be fabricated next to each other on the same wafer (Figure 1a). Planar wafer-level fabrication imposes a single, fixed spacer thickness across all devices. As a result, reflection suppression can be satisfied only for one device—or at best a small subset—while the remaining devices become detuned from the reflectionless condition and suffer increased reflection and reduced efficiency. Addressing this scalability challenge is the central motivation of the present work.

Here, we design a terahertz bilayer setting in which by employing rotational symmetry and Lorentz reciprocity, the reflection suppression becomes invariant with respect to both the relative twist angle and the spacer thickness. This enables near-zero reflection at the resonance frequency for all polarization rotation angles using a single, common spacer thickness, which is essential for wafer-scale fabrication of structured-polarization components. Moreover, our design achieves linear polarization rotation without inducing ellipticity while maintaining reflection suppression, a combination that becomes increasingly difficult to realize in twisted bilayer systems as the rotation angle varies. Table 1 summarizes these distinctions and highlights that the present approach uniquely combines polarization-independent near-zero reflection, compatibility with multiple rotation angles on the same wafer while making sure thickness-invariant reflectionless operation, capabilities that have not been achieved simultaneously in prior bilayer chiral metasurface platforms.

Concept and Theory

The conceptual illustration of the design principle for our high-efficiency polarization rotator, with in-demand rotation angles, has been illustrated in Figure 1b. To realize polarization-independent rotators with angular robustness, we exploit a geometry having 4-fold in-plane rotational symmetry. This symmetry enforces identical electromagnetic response for any incident linear polarization, independent of orientation of incident linear state, thereby removing azimuthal dependence. However, a single-layer implementation with C_4-symmetry device cannot produce polarization rotation, because it is effectively nonbirefringent: orthogonal polarizations experience nearly identical effective indices, leaving no in-plane differential phase to drive rotation. To overcome this limitation, we utilize a bilayer configuration in which two identical arrays of split-ring resonators (SRRs) are stacked with a relative in-plane twist. This arrangement breaks mirror symmetry and induces structural chirality, which is essential for enabling polarization rotation. We should note that the presence of 4-fold rotational symmetry together with Lorentz reciprocity, removes cross-polarization reflection and reduces the reflection suppression to only copolarization component. This concept is formulated using a general 4 × 4 scattering-matrix formalism that relates the outgoing field components (E^o) to the incoming ones (E^i), $\boldsymbol{E}^o = S\boldsymbol{E}^i$, or explicitly

$$\begin{bmatrix} E^o_{1x} \\ E^o_{1y} \\ E^o_{2x} \\ E^o_{2y} \end{bmatrix} = \begin{bmatrix} R^{xx}_{11} & R^{xy}_{11} & T^{xx}_{12} & T^{xy}_{12} \\ R^{yx}_{11} & R^{yy}_{11} & T^{yx}_{12} & T^{yy}_{12} \\ T^{xx}_{21} & T^{xy}_{21} & R^{xx}_{22} & R^{xy}_{22} \\ T^{yx}_{21} & T^{yy}_{21} & R^{yx}_{22} & R^{yy}_{22} \end{bmatrix} \begin{bmatrix} E^i_{1x} \\ E^i_{1y} \\ E^i_{2x} \\ E^i_{2y} \end{bmatrix} \tag{1}$$

We now consider the action of a C_4 in-plane rotation. In the chosen polarization basis, the corresponding rotation matrix is

$$\mathrm{R} = \begin{bmatrix} 0 & -1 & 0 & 0 \\ 1 & 0 & 0 & 0 \\ 0 & 0 & 0 & -1 \\ 0 & 0 & 1 & 0 \end{bmatrix} \tag{2}$$

If the structure possesses C_4 rotational symmetry, the scattering matrix must be invariant under this rotation, which imposes the condition $R^{-1}SR = S$ and takes the following form

$$\begin{bmatrix} R^{yy}_{11} & -R^{yx}_{11} & T^{yy}_{12} & -T^{yx}_{12} \\ -R^{xy}_{11} & R^{xx}_{11} & -T^{xy}_{12} & T^{xx}_{12} \\ T^{yy}_{21} & -T^{yx}_{21} & R^{yy}_{22} & -R^{yx}_{22} \\ -T^{xy}_{21} & T^{xx}_{21} & -R^{xy}_{22} & R^{xx}_{22} \end{bmatrix} = \begin{bmatrix} R^{xx}_{11} & R^{xy}_{11} & T^{xx}_{12} & T^{xy}_{12} \\ R^{yx}_{11} & R^{yy}_{11} & T^{yx}_{12} & T^{yy}_{12} \\ T^{xx}_{21} & T^{xy}_{21} & R^{xx}_{22} & R^{xy}_{22} \\ T^{yx}_{21} & T^{yy}_{21} & R^{yx}_{22} & R^{yy}_{22} \end{bmatrix} \tag{3}$$

This equality imposes strong constraints on both the reflection and transmission matrices. Focusing on the reflection blocks, C_4 rotational symmetry enforces equality of the copolarized reflection coefficients along the two orthogonal axes, i.e., $R^{xx}_{11} = R^{yy}_{11}$ and $R^{xx}_{22} = R^{yy}_{22}$. As an arbitrary input polarization can be decomposed into orthogonal x and y components, this condition ensures that both components experience the same copolarized reflectivity, independent of the incident polarization angle. Consequently, the device exhibits polarization-independent copolarized reflection. In addition, C_4 symmetry requires the cross-polarized reflection terms to be antisymmetric, $R^{xy}_{11} = -R^{yx}_{11}$ and $R^{xy}_{22} = -R^{yx}_{22}$.

After equating all terms in eq 1, the scattering matrix subject to C_4 rotational symmetry takes the form

$$S = \begin{bmatrix} R^{xx}_{11} & R^{xy}_{11} & T^{xx}_{12} & T^{xy}_{12} \\ -R^{xy}_{11} & R^{xx}_{11} & -T^{xy}_{12} & T^{xx}_{12} \\ T^{xx}_{21} & T^{xy}_{21} & R^{xx}_{22} & R^{xy}_{22} \\ -T^{xy}_{21} & T^{xx}_{21} & -R^{xy}_{22} & R^{xx}_{22} \end{bmatrix} \tag{4}$$

On the other hand, the system is linear, passive, and reciprocal. Lorentz reciprocity therefore requires the scattering matrix to be symmetric, $S = S^T$. This additional constraint forces the cross-polarized reflection coefficients to vanish, i.e., $R^{xy}_{11} = R^{xy}_{22} = 0$. The resulting scattering matrix reduces to

$$S = \begin{bmatrix} R^{xx}_{11} & 0 & T^{xx}_{12} & T^{xy}_{12} \\ 0 & R^{xx}_{11} & -T^{xy}_{12} & T^{xx}_{12} \\ T^{xx}_{21} & T^{xy}_{21} & R^{xx}_{22} & 0 \\ -T^{xy}_{21} & T^{xx}_{21} & 0 & R^{xx}_{22} \end{bmatrix} \tag{5}$$

https://doi.org/10.1021/acsomega.5c11042
ACS Omega 2026, 11, 6264−6274

As a consequence, reflection suppression is no longer limited by polarization-conversion channels. Instead, it is governed solely by the copolarized reflection coefficient R_{11}^{xx} and R_{22}^{xx} which is identical for all input polarization states due to C_4 symmetry. Therefore, achieving polarization-independent reflectionless operation reduces to enforcing $R_{11}^{xx} = R_{22}^{xx} = 0$.

To achieve zero reflectivity, we rely on interference effects in bilayer system. We therefore model the structure as a bilayer setting consisting of two generic layers separated by a spacer of thickness d. Under C_4 symmetry and reciprocity, the copolarized reflection blocks of each layer are proportional to the identity matrix, while the cross-polarized reflection terms vanish. As a result, the copolarized reflection response reduces to a scalar quantity, and the bilayer could be analyzed using a scalar multiple-scattering formulation.

Let r_1 and t_1 denote the copolarized reflection and transmission coefficients of the front layer for incidence from the front side and let r_1' denote the copolarized reflection coefficient of the same layer for incidence from the spacer side. Let r_2 denote the copolarized reflection coefficient of the back layer as seen from the spacer. Propagation through a lossless spacer introduces the complex phase factor $e^{-i\beta}$, $\beta = k_0 nd$ with k_0 as free space wavevector and n as the refractive index of the spacer medium.

With illumination only from the front, the total copolarized reflection is the superposition of: (i) the direct reflection from the front layer, and (ii) all components that transmit through the front layer, reflect from the back layer, and undergo multiple round trips between the two layers. Explicitly,

$$r_{tot} = r_1 + t_1^2 r_2\, e^{-i2\beta}[1 + r_1' r_2\, e^{-i2\beta} + (r_1' r_2\, e^{-i2\beta})^2 + \cdots] \tag{6}$$

The bracketed term is a geometric series and can be summed exactly, yielding the closed-form expression

$$r_{tot} = r_1 + \frac{t_1^2 r_2\, e^{-i2\beta}}{1 - r_1' r_2\, e^{-i2\beta}} \tag{7}$$

Eq 6 includes all multiple reflections between the two layers. The reflectionless condition arises from destructive interference between two physically distinct copolarized reflection pathways. The first contribution is the field reflected directly by the front layer, with complex amplitude r_1. The second contribution is the field that is transmitted through the front layer, reflected by the back layer, and then transmitted back to the input side after one or more round trips across the spacer. The total contribution of this second pathway is captured by the second term in eq 6. Reflection suppression occurs when these two complex amplitudes cancel each other, i.e., $r_{tot} = 0$ at a resonance frequency which requires both an amplitude balance and a phase difference of π between the direct front reflection r_1 and the effective back-reflection pathway.

We further note that, because the reflection block is proportional to the identity matrix, it remains invariant under in-plane rotation of the layers relative to each other. Consequently, once the spacer thickness d is chosen to yield zero reflectivity, this condition remains valid for all relative twist angles between the two layers. This invariance of the reflectionless condition with respect to layer rotation is described in more detail below.

Using the reduced scattering matrix obtained under C_4 symmetry and reciprocity, the front-side reflection block takes the form

$$R_{11} = R_{11}^{xx} I_2, \qquad I_2 = \begin{bmatrix} 1 & 0 \\ 0 & 1 \end{bmatrix} \tag{8}$$

Now consider rotating only one layer in the plane by an angle α. In the linear polarization basis, this rotation is represented by

$$D(\alpha) = \begin{bmatrix} \cos(\alpha) & -\sin(\alpha) \\ \sin(\alpha) & \cos(\alpha) \end{bmatrix},$$
$$D^{-1}(\alpha) = \begin{bmatrix} \cos(\alpha) & \sin(\alpha) \\ -\sin(\alpha) & \cos(\alpha) \end{bmatrix} \tag{9}$$

After rotation, the reflected field is obtained by first rotating the polarization components into the rotated frame, applying the reflection matrix, and then rotating back. The resulting reflection block is therefore

$$R_{11}(\alpha) = D(\alpha) R_{11} D^{-1}(\alpha) \tag{10}$$

Substituting eq (A1) into eq (A3) gives

$$\begin{aligned} R_{11}(\alpha) &= D(\alpha)[R_{11}^{xx} I_2] D^{-1}(\alpha) \\ &= R_{11}^{xx} D(\alpha) I_2 D^{-1}(\alpha) \end{aligned} \tag{11}$$

Since I_2 leaves any vector unchanged and $D(\alpha)D^{-1}(\alpha) = I_2$, we obtain

$$R_{11}(\alpha) = R_{11}^{xx} I_2 = R_{11} \tag{12}$$

Therefore,

$$R_{11}^{xx}(\alpha) = R_{11}^{xx} \tag{13}$$

which shows that the copolarized reflection coefficient is unchanged by relative twist between layers. In contrast, the transmission blocks are not proportional to the identity matrix and therefore change under rotation, allowing polarization conversion in transmission while leaving the reflectionless condition $R_{11}^{xx} = 0$ unaffected.

Design and Simulation

Figure 1c illustrates a schematic representation of a single unit cell from the periodic bilayer design. Each layer of the metasurface is composed of four identical SRRs arranged in a square lattice. Applying a relative angular offset, α, on the resonators of one layer relative to the other, chirally couples the two metasurfaces, producing the desired polarization-rotating response. Importantly, this angular twist, α, preserves the overall C_4 rotational symmetry of the structure. The use of 4-fold rotational symmetry serves a dual purpose: it guarantees polarization independence of the transmission, and it suppresses all cross-polarized reflection over the entire spectral range.[50−52] The design challenge in annihilating reflectivity then reduces to eliminating copolarized reflection (Figure 1b), which is achieved via destructive interference of the reflected fields. The interlayer separation is thus tuned such that this cancellation occurs at a target resonance, yielding an effectively reflectionless and narrowband polarization rotation.

Our periodic structure was modeled using the RF Module of COMSOL Multiphysics. Bloch (Floquet) boundary conditions were applied to the lateral walls of the unit cell, while input and output ports were used to launch and collect continuous plane-waves. The SRRs were modeled as copper films (conductivity $\sim 6 \times 10^7$ S/m, thickness 1 μm) patterned on polyimide layers with relative permittivity $\varepsilon_r \sim 3.15$. The array periodicity was

https://doi.org/10.1021/acsomega.5c11042
ACS Omega 2026, 11, 6264−6274

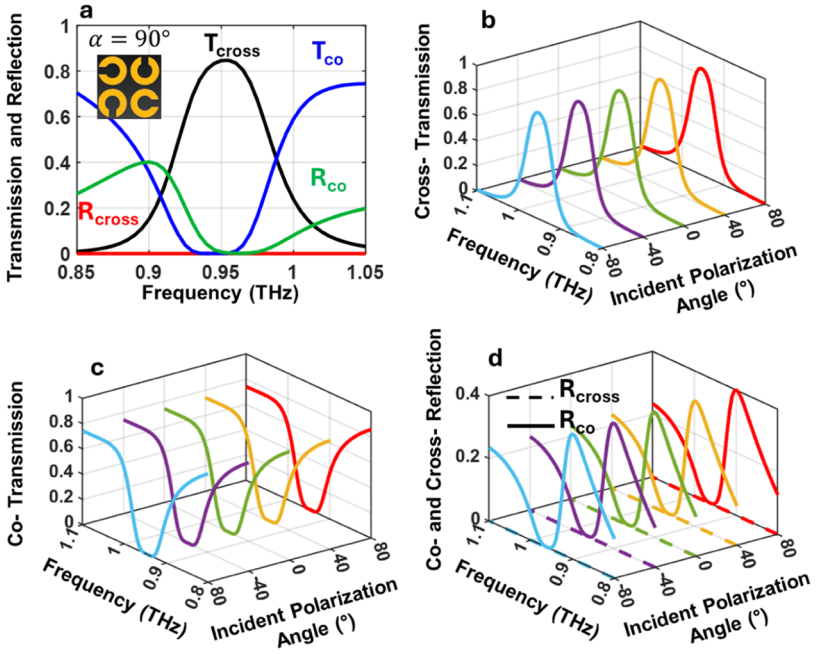

Figure 2. (a) Reflection and transmission spectra of the cross-polarization converter for an incident polarization angle of 0°. The inset shows the front layer of the metasurface with a twist angle of α = 90°. (b) and (c) Cross- and copolarized transmission spectra for several incident linear polarization orientations, respectively. (d) Cross- and copolarized reflection spectra for the same input polarizations, shown respectively with dashed and solid lines.

set to 140 μm, with inter-SRR spacing of ∼43 μm. The SRRs had an inner radius and gap dimension of 10 μm and a ring width of 9 μm.

The initial interlayer twist angle α was selected as 90°. The polyimide layer thickness was then optimized to 38 μm, ensuring destructive interference of copolarized reflection at the target resonance (∼0.95 THz). Later, the twist angle was varied to analyze the device response for other rotations. The entire design uses geometry and materials compatible with standard photolithographic fabrication.[53] As shown in Figure 1c, but for much more clarity, we now summarize the geometric parameters of the metasurface unit cell used in simulations. The structure consists of two polyimide layers supporting the split-ring resonators (SRRs) and one polyimide capping layer, each with a thickness of 38 μm. The copper SRRs have a thickness of 1 μm, an inner radius of 10 μm, a gap size of 10 μm, and a ring width of 9 μm. The total device thickness is therefore given by the sum of all polyimide and metal layers, 38 μm + 38 μm + 38 μm + 1 μm + 1 μm = 116 μm. The unit-cell periodicity is 140 μm, and the inter-SRR spacing is equal to 43 μm. Additionally, to evaluate the output polarization state, we calculated the polarization ellipse from the in-plane electric field components. The polarization ellipse fully characterizes the output polarization through its orientation (φ) and ellipticity (χ) angles. For a monochromatic wave propagating along z, the transverse electric field traces an ellipse in the x−y plane. The orientation angle φ specifies the direction of the ellipse's major axis relative to the x-axis, while χ quantifies the ellipticity, distinguishing linear from elliptical polarization. The orientation angle and ellipticity are defined by the following equations: $\tan(2\varphi) = 2E_x E_y \cos(\delta)/(E_x^2 - E_y^2)$ and $\sin(2\chi) = 2E_x E_y \sin(\delta)/(E_x^2 + E_y^2)$, where E_x and E_y are the amplitude of the electric field components along the x- and y-axes, and δ is their relative phase difference.[54]

From now on in this paper, we will use the terms co- to refer to the reflected or transmitted wave components that are in the same direction with the input polarization, while the term cross indicates to those that are orthogonal to the input polarization. For example, for an x-polarized incident wave, the T_{cross} and R_{cross} components correspond to the y-polarized transmitted and reflected waves, respectively, whereas the T_{co} and R_{co} components represent the x-polarized transmitted and reflected waves.

RESULTS AND DISCUSSION

We first designed and analyzed a device targeting a narrowband 90° polarization rotation at normal incident angle. Figure 2a shows the frequency-dependent transmission and reflection characteristics for this device, with the inset illustrating the front layer of the unit cell at α = 90°. The most notable feature is the cross-transmission (T_{cross}) response (dark line), which exhibits a sharp resonance near 0.95 THz with a peak conversion amplitude of ∼85%. The remaining power is dissipated as ohmic loss in the copper SRRs. This strong conversion efficiency arises from two key design principles: (i) the 4-fold rotational symmetry, which suppresses cross-polarized reflection (R_{cross}) across the entire spectrum (red curve), and (ii) destructive interference, achieved by judiciously tuning the interlayer spacing, which reduces copolarized reflection (R_{co}) to nearly zero at the resonance frequency (green line). Together with the structural chirality introduced by the 90° twist, the device transforms an incident horizontal polarization almost entirely into its orthogonal counterpart. This is confirmed by the suppression of copolarized transmission, i.e., T_{co}, to ∼0% (green line) and the survival of only cross-polarized transmission (T_{cross}).

To demonstrate the polarization-independent characteristics of this device we analyzed the response at different input linear polarization states. The cotransmission (T_{co}) spectrum as a

https://doi.org/10.1021/acsomega.5c11042
ACS Omega 2026, 11, 6264−6274

function of the incident polarization angle, which is systematically changed from −80° to +80° is shown in Figure 2b. The data set's most important finding is the invariance of the device's response across the whole range of incident angles. This reliable performance demonstrates that the device's orthogonal polarization conversion efficiency is completely independent of the input polarization state, a critical feature for applications where the incident polarization may be random or unknown. Figure 2c, which shows the cotransmission (T_{co}) spectrum under the same sweeping polarization conditions, provides a more thorough validation of this polarization-independent operation. This comprehensive examination is completed by the metamaterial's reflection characteristics, shown in Figure 2d. The data make evident that the exceptionally low values for both co- and cross-reflection remain close to zero for every incident polarization angle applied. All these results are a clear indication of azimuthal-free response of the designed arrangement.

The state of the transmitted polarization for this cross-rotator device is presented in Figure 3. Figure 3a illustrates the

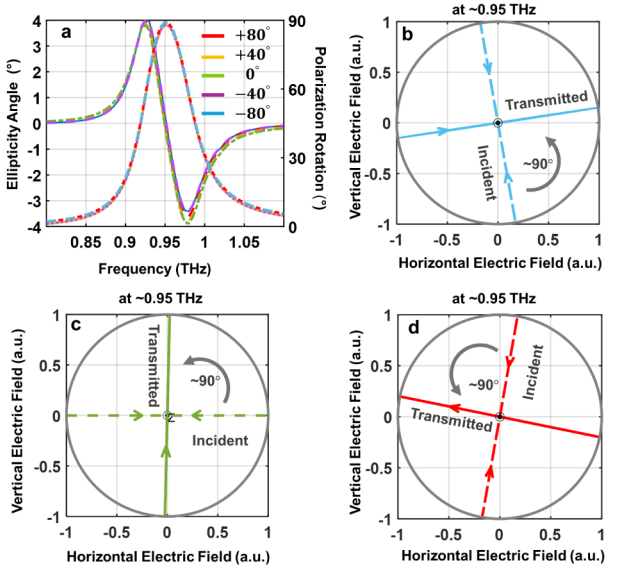

Figure 3. (a) Polarization rotation and ellipticity (in degrees) of the transmitted wave as a function of frequency for various incident polarization angles ranging from −80° to +80°. (b), (c), and (d) Polarization ellipse diagrams at ~0.95 THz, visually depicting the incident (dashed lines) and transmitted (solid lines) polarization states for input polarizations of −80°, 0°, and 80°, respectively. These figures clearly illustrate the consistent ~90° rotation of the linear polarization, independent of input polarization orientation.

polarization rotation (φ) and ellipticity (χ) in degrees for the output wave as a function of frequency, plotted for several incident linear polarizations ranging from −80° to 80°. The full spectral overlap across all incident angles signifies the device's robust independence from the input polarization azimuth. The clear resonant shift at ~0.95 THz signifies a ~90° polarization rotation relative to the incident field. Simultaneously, at this resonance frequency, the ellipticity remains close to zero (<0.6°), which is a vital metric confirming the near perfect linear polarization conversion. This high-quality transformation is further verified by the shape of the polarization ellipses. Figure 3b–d provides visual evidence of this unique performance at the resonant frequency of ~0.95 THz for three representative input orientations, namely −80, 0, and 80°. In Figure 3b, the incident field at −80° (dashed line) is shown alongside the transmitted field (solid line). It clearly illustrates that an 80-degree linear polarization is effectively rotated by ~90°. Figure 3c extends this analysis by demonstrating an incident wave at 0°, which is then rotated to an output polarization at ~90°, thus showing a consistent cross transformation. Similarly, Figure 3d depicts an incident field at +80° being rotated to an output field at 170°, again confirming the robust cross-polarization conversion for variety of linear input states.

Once the performance of the 90° rotator was verified, we extended the study to devices with alternative twist angles, α. Figure 4a,b shows the reflection spectra for two representative

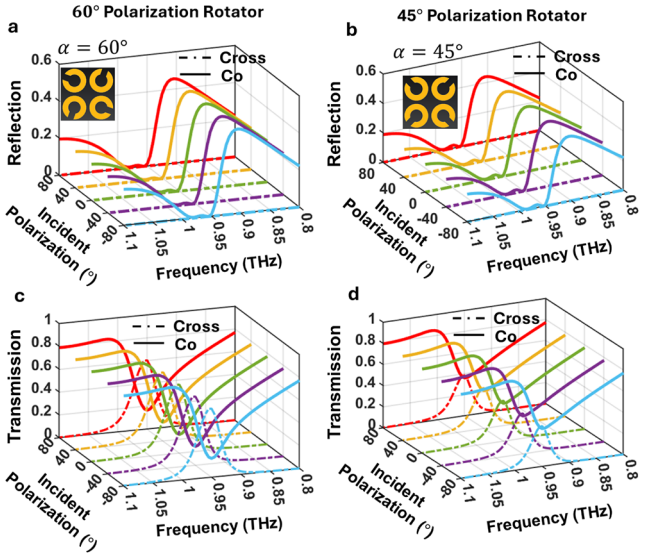

Figure 4. (a) and (b) Reflection spectra for the 60° and 45° rotators, respectively, for several input polarizations. The insets display the front layer of the unit cells, illustrating a distinct relative twist angle (α), applied to the front SRRs. In both cases, the cross reflectivity (dashed lines) vanishes across the full frequency range, and the copolarized reflection (solid lines) is strongly suppressed near the resonant frequency ~0.95 THz, regardless of input polarization. (c) and (d) Polarization independent, transmission versus frequency for the 60° and 45° rotators, respectively. The cross-polarized components are plotted as dashed lines, while the copolarized parts are shown as solid lines.

devices, i.e., 60° and 45° rotators, respectively. In both cases, the dashed curves represent cross-polarized reflection (R_{cross}), while the solid lines correspond to copolarized reflectivity (R_{co}). The insets illustrate the front layer of the unit cell configurations, where the main distinction is the twist angle (α = 60° versus 45°). This angle, together with small adjustments of the in-plane SRR spacing (l), sets the prescribed rotation and ensures optimal polarization conversion efficiency. As seen from these figures, the cross-reflection remains negligible across the entire spectrum, whereas the coreflectivity is strongly suppressed at the resonance frequency of ~0.95 THz, consistent with the 90° device. This suppression persists across all input polarization orientations, evidenced from the identical spectra for all input states, confirming the azimuthal robustness of the design.

Figure 4c,d represents the transmission spectra for the same devices, with dashed lines indicating cross-polarized compo-

https://doi.org/10.1021/acsomega.5c11042
ACS Omega 2026, 11, 6264−6274

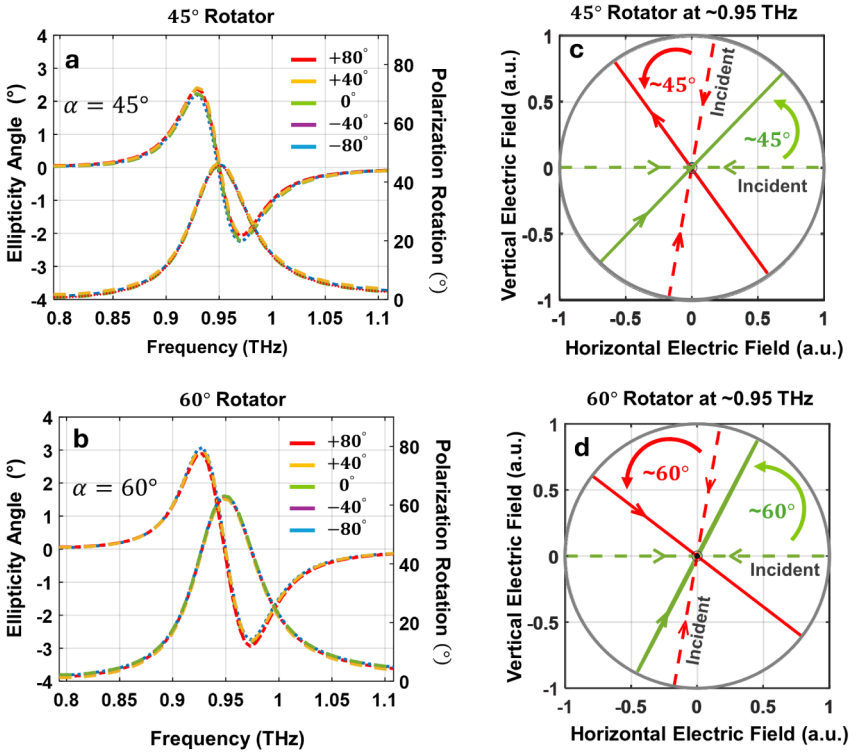

Figure 5. (a) and (b) Polarization rotation and ellipticity spectra for the 45° and 60° rotators, respectively, for a few selected input states from −80° to +80°. The ellipticity remains close to zero at 0.95 THz in both rotators independent of input angles. (c) and (d) Polarization-state diagrams for the 45° and 60° devices at ∼0.95 THz, shown for two representative input orientations of 0° (green) and 80° (red). Dashed lines denote the incident states, while solid lines show the transmitted polarizations, which are rotated by ∼45° and ∼60° while maintaining their near-linear status.

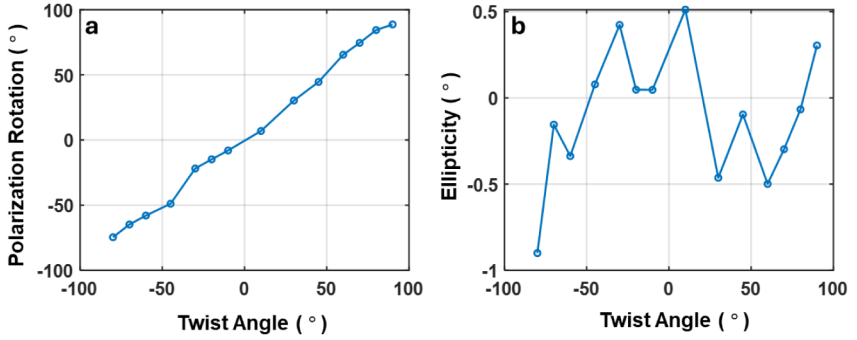

Figure 6. (a) Polarization rotation of transmitted wave versus twist angle, α, for 0° input polarization. (b) The corresponding ellipticity as a function of twist angle, α, for the same incident wave. Similar behavior is expected for other input polarization angles due to the device's invariant azimuthal response.

nent (T_{cross}) and solid lines showing copolarized outputs (T_{co}). At the resonance, the 45° rotator produces nearly equal co- and cross- output intensities, as expected for a 45° transformation, while the 60° rotator yields unequal magnitudes consistent with its design. These results, collectively, confirm that the metasurface achieves a reflectionless operation and polarization-independent performance across multiple rotation angles at the operating frequency of ∼0.95 THz. This performance is obtained without any change in the layers or overall device thickness. This thickness-invariant property ensures that arrays of devices with different rotation angles can be processed on the same wafer, all exhibiting similar reflectionless performance at a common operating frequency.

To characterize the polarization rotation capability of these metasurface devices, we extracted the rotation angle (φ) and ellipticity (χ) from the simulated electric fields, incorporating both amplitude and phase information. Figure 5a,b depicts the frequency-dependent polarization rotation and ellipticity for the 45° and 60° rotators, respectively. For each device, the spectra corresponding to several incident polarization angles overlap almost perfectly, demonstrating that the rotation action is independent of the input polarization.

At the resonance frequency, the ellipticity remains below 0.5°, implying that the transmitted field retains a near-linear state. The observed ∼45° and ∼60° rotation angles occur at the same resonant frequency and are primarily governed by the designed twist angle α. The polarization-plane diagrams in Figure 5c,d provides a visual representation of this behavior, showing how the transmitted polarization states for two representative input orientations (0° and 80°) undergo a clear

https://doi.org/10.1021/acsomega.5c11042
ACS Omega 2026, 11, 6264−6274

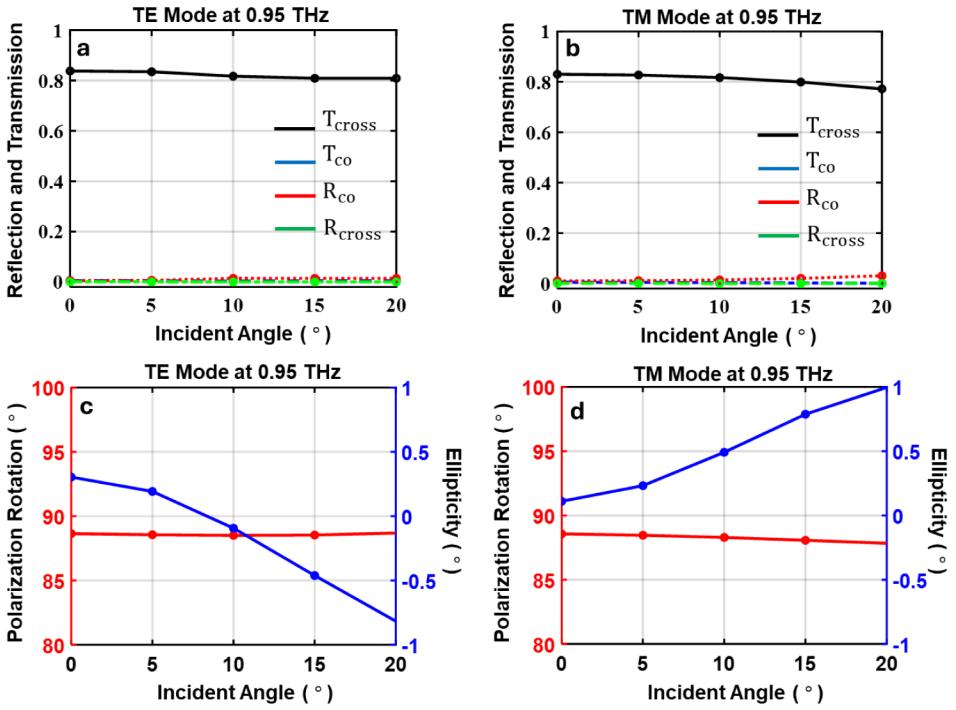

Figure 7. (a) and (b) Transmission and reflection spectra at ∼0.95 THz as a function of incident angle for TE and TM modes, respectively. (c) and (d) Calculated polarization rotation (red) and ellipticity (blue) versus incident angle for TE and TM waves, respectively. The rotation remains close to 90°, while the ellipticity increases only slightly, reaching ∼1° at 20° incidence.

and consistent rotation at the resonance. In these plots, the dashed lines indicate the incident polarization states, while the solid lines mark the corresponding transmitted ones. For the 45° rotator, the incident linear fields are rotated to new eigenstates by ∼45°, while for the 60° device the transmitted polarization is rotated by ∼60°. In both cases, the polarization trajectories confirm near-linear conversion with negligible ellipticity. Together, these results validate that the proposed metasurface can realize controllable, thickness-invariant linear polarization rotation with high fidelity, where the output angle is prescribed primarily by the structural twist, α.

To extend the analysis beyond the three representative devices, we comprehensively evaluated the reflectionless polarization rotation action of our device for several other twist angles, while maintaining the constant layers' thickness. Figure 6a shows the polarization rotation versus α at ∼0.95 THz, demonstrating that the rotated angle of the transmitted beam closely follows the structural mechanical twist across a wide range from −90° to +90°.

These results confirm that the desired rotation angles can be lithographically defined by selecting the twist parameter, α, across multiple rotators, without modifying the layer thickness or material composition. Consequently, all devices can be fabricated within a single, uniform process flow. Although the data in Figure 6 were plotted for a single input polarization orientation (0°), the device is inherently azimuthally invariant as demonstrated in the previous analysis, ensuring the same behavior for all input polarizations. To verify linearity of the output fields, Figure 6b represents the corresponding ellipticity values obtained across the same range of twist angles. The magnitude of ellipticity remains below 0.9 degrees, verifying that the transmitted wave preserves a high degree of linearity regardless of the physical twist. Importantly, in all these simulations the total reflectivity remains small, signifying that the polarization rotation occurs with negligible reflection losses. Together, these results establish that the metasurface operates as a thickness-invariant, reflectionless, and polarization-independent platform in which the rotation is virtually set by the twist angle while maintaining near-linear polarization state.

Finally, we analyzed the stability of the device with respect to oblique incidence for the 90° device. Figure 7a,b represents the transmission and reflection at ∼0.95 THz versus incident angle for TE and TM waves, respectively. In both cases, the cross-polarized transmission (dark curves) remains as high as 78% to 85%, while all other polarization components in both reflection and transmission are negligible. This behavior persisted for incident angles up to ∼0°. The corresponding polarization rotation (red curves) and ellipticity (blue lines) are plotted in Figure 7c,d for the same TE and TM incidence, respectively. The polarization rotation angle stays close to ∼90°, while the ellipticity increases, reaching ∼1° at ∼20° incident angle. These results confirm that the device sustains its robust performance up to an oblique incidence angle of ∼20°.

Although the present work is based on numerical design and simulation, the proposed metasurface can be fabricated using standard planar microfabrication techniques. A feasible process flow is outlined as follows. The process begins with a silicon substrate onto which a polyimide layer is spin-coated, soft-baked, and subsequently thermally cured in a vacuum oven to form the base dielectric layer. A positive-tone photoresist is then applied and patterned via photolithography, followed by development to define the SRR pattern. Copper is deposited using either e-beam evaporation or sputtering, and a liftoff step is performed to retain Cu only in the patterned SRR regions. Next, a second polyimide layer is spin-coated and soft-baked. To ensure alignment with the first layer, a localized acetone

https://doi.org/10.1021/acsomega.5c11042
ACS Omega 2026, 11, 6264−6274

Table 2. Sensitivity of Cross Polarizer to the Twist Angle

Twist angle error	Polarization Rotation Angle	Ellipticity	T_{cross}	T_{co}	R_{co}	R_{cross}
+5°	95°	0.34°	0.83845	0.0007	0.004	0.0005
0°	90°	0.78°	0.8377	0.005	0.005	0.0007
−5°	85°	0.62°	0.8259	0.018	0.010	0.00001

swab (followed by an IPA rinse) can be applied to expose alignment marks from the previous layer. After curing this layer, the second SRR pattern is defined through photolithography, development, Cu deposition, and liftoff, following the same procedure as the first. A final encapsulation layer of polyimide is spin-coated, soft-baked, and cured. To release the device from the silicon substrate, the cured polyimide film can be mechanically peeled off.[53] Alternatively, the wafer can be coated with a protective photoresist on both sides, and backside photolithography can be used to open an aperture aligned to the patterned region. The exposed silicon can then be selectively etched in a wet etchant until the polyimide interface is reached, yielding a free-standing bilayer metasurface film supported by the Si wafer.

To assess fabrication tolerance, we evaluated the sensitivity of the 90° cross-polarization rotator to realistic twist-angle deviations of ±5°. The results in Table 2 show that the polarization rotation angle changes approximately linearly with the imposed twist error ($\Delta\varphi \sim \Delta\alpha$), while the transmitted polarization remains predominantly linear with ellipticity $|\chi| < 1$. Importantly, the cross-polarized transmission remains high ($T_{cross} \sim 0.83-0.84$), and both co- and cross-polarized reflections stay near zero.

We also investigated the impact of realistic polyimide interlayer spacing variations (±2−3 μm), which commonly arise in spin-coated films, on the performance of the 90° cross-polarization rotator. The results are summarized in Table 3. It

Table 3. Sensitivity of Cross Polarizer to the Polyimide Thickness

Resonance Frequency (THz)	T_{cross}	Reflection	Polyimide Thickness (μm)
0.96	0.84	0.003	40
0.96	0.85	0.001	39
0.965	0.85	0.003	38
0.975	0.84	0.012	37.6
0.975	0.84	0.022	37
0.98	0.84	0.000	36

shows that such spacing deviations primarily cause a shift in resonance frequency within a range of 0.96 to 0.98 THz, while the cross-polarized transmission remains high and stable. Simultaneously, reflection remains very low (<0.025) and approaches near-zero at the nominal design spacing, indicating that the destructive-interference condition responsible for reflection suppression is preserved. These findings demonstrate that the device maintains both efficient polarization conversion and near reflectionless operation under practical fabrication-level spacing variations.

Finally, to evaluate the effect of ohmic loss from the copper in cross polarizer device, we systematically reduced the conductivity of copper in the simulations. As seen in Table 4, decreasing conductivity leads to a reduction in cross-polarized transmission efficiency, while the device continues to maintain low reflection and keeps its linear cross-polarization

Table 4. Sensitivity of Cross Polarizer to the Copper Conductivity

Conductivity (S/m)	T_{co}	R_{co}	R_{cross}	T_{cross}
6×10^7	0.005232	0.005861	7.76×10^{-4}	0.8377
3×10^7	0.007551	0.002216	3.87×10^{-4}	0.55213
1.5×10^7	0.00555	0.004212	6.05×10^{-4}	0.71921

operation. This behavior confirms that ohmic loss primarily limits efficiency rather than polarization functionality. Importantly, even under elevated loss conditions, the metasurface preserves its 90° linear-to-linear polarization rotations, demonstrating robustness of the underlying interference and symmetry-based mechanism against realistic ohmic losses.

Limitations and Scope

While the proposed approach enables thickness-invariant, reflection-suppressed rotation, several practical limitations should be noted. First, the demonstrated operation is inherently narrowband, with reflection suppression and polarization rotation occurring only in the vicinity of the designed resonance frequency (≈0.95 THz). Second, the present design is limited to linear-to-linear polarization rotation; extension to arbitrary polarization states or broadband ellipticity control is beyond the scope of this work. Third, the device performance degrades for oblique incidence, with noticeable reduction in efficiency beyond incidence angles of approximately 20°, due to the breakdown of normal-incidence symmetry assumptions. In addition, the bilayer configuration requires precise interlayer alignment, and misalignment can introduce unwanted coupling and reduce conversion efficiency. Finally, ohmic losses in the copper resonators limit the experimentally achievable efficiency, particularly at terahertz frequencies. These constraints define the current scope of applicability of the proposed design and highlight directions for future improvement, such as broadband implementations, alternative low-loss materials, and relaxed alignment tolerances.

CONCLUSION

In this work, we demonstrated a metasurface arrangement for universal, reflectionless, and polarization-independent linear rotators. By employing a bilayer C_4 symmetric design, cross-polarized reflection is eliminated across the spectrum, while destructive interference suppresses copolarized reflection at the operating resonance frequency. This mechanism enables a high-efficiency transmission with negligible reflection losses, independent of the input polarization orientation. Numerical simulations confirmed that the rotation angle is governed primarily by a relative twist between the two layers, allowing arbitrary polarization rotations to be lithographically prescribed without requiring changes in device thickness. The transmitted waves remain nearly linear, with ellipticity values close to zero across a wide range of twist angles. In addition, the rotators maintain their performance up to ∼20° oblique incidence for both TE and TM illumination, further highlighting their robustness. These results establish a thickness-invariant, azimuthally independent, and angle-tolerant ap-

https://doi.org/10.1021/acsomega.5c11042
ACS Omega 2026, 11, 6264−6274

proach to polarization rotation that is scalable across optical, infrared, and terahertz frequencies. Such devices provide a compact and lithographically compatible alternative to bulky natural crystals, opening opportunities for integrated photonic systems in areas including secure communications, beam shaping, polarimetric imaging, and advanced optical signal processing.

AUTHOR INFORMATION

Corresponding Author

Mohammad Parvinnezhad Hokmabadi − *Electrical and Computer Engineering Department, University of North Carolina at Charlotte, Charlotte, North Carolina 28223, United States;* orcid.org/0000-0001-9705-1282; Email: mparvinn@charlotte.edu

Authors

Hadi Ahmadi − *Electrical and Computer Engineering Department, University of North Carolina at Charlotte, Charlotte, North Carolina 28223, United States*

Sanchita Sarker − *Electrical and Computer Engineering Department, University of North Carolina at Charlotte, Charlotte, North Carolina 28223, United States*

Complete contact information is available at: https://pubs.acs.org/10.1021/acsomega.5c11042

Author Contributions

All authors contributed equally to this work.

Notes

The authors declare no competing financial interest.

ACKNOWLEDGMENTS

We acknowledge FRG and GASP financial support from UNC Charlotte.

REFERENCES

(1) Snik, F.et al.An overview of polarimetric sensing techniques and technology with applications to different research fields*Polarization: measurement, Analysis, And Remote Sensing XI.9099*SPIE201448−67

(2) Shurcliff, W. A. *Polarized light: production and use*; Harvard University Press, 1962.

(3) Wang, L.; Zimnyakov, D. *Optical polarization in biomedical applications*; Springer: New York, 2006; Vol. *467*.

(4) Giuli, D. Polarization diversity in radars. *Proc. IEEE* **2005**, *74* (2), 245−269.

(5) Yang, Y.; Seong, J.; Choi, M.; Park, J.; Kim, G.; Kim, H.; Jeong, J.; Jung, C.; Kim, J.; Jeon, G.; et al. Integrated metasurfaces for re-envisioning a near-future disruptive optical platform. *Light Sci Appl.* **2023**, *12* (1), 152.

(6) Rubin, N. A.; D'Aversa, G.; Chevalier, P.; Shi, Z.; Chen, W. T.; Capasso, F. Matrix Fourier optics enables a compact full-Stokes polarization camera. *Science* **2019**, *365* (6448), No. eaax1839.

(7) Mironov, E. A. Elimination of depolarization in a Faraday isolator based on a rotator with natural optical activity. *Opt. Lett.* **2025**, *50* (16), 4982−4985.

(8) Porta, A. L.; Wang, M. D. Optical Torque Wrench: Angular Trapping, Rotation, and Torque Detection of Quartz Microparticles. *Phys. Rev. Lett.* **2004**, *92* (19), 190801.

(9) Al-Mahmoud, M.; et al. Broadband polarization rotator with tunable rotation angle composed of three wave plates. *Phys. Rev. Appl.* **2020**, *13* (1), 014048.

(10) Hu, Y.; et al. All-dielectric metasurfaces for polarization manipulation: principles and emerging applications. *Nanophotonics* **2020**, *9* (12), 3755−3780.

(11) Zhou, C.; et al. Polarization guided HDR reconstruction via pixel-wise depolarization. *IEEE Trans. Image Process* **2023**, *32*, 1774−1787.

(12) Vogliardi, A.; Ruffato, G.; Bonaldo, D.; Dal Zilio, S.; Romanato, F.; et al. Azimuthally-variant perfect vector beams for the control of arbitrary phase and polarization ring patterns. *Light Sci Appl.* **2025**, *14* (1), 183.

(13) Zhang, C.; et al. High efficiency all-dielectric pixelated metasurface for near-infrared full-Stokes polarization detection. *Photonics Res.* **2021**, *9* (4), 583−589.

(14) Cong, L; Cao, W; Zhang, X; Tian, Z; Gu, J; Singh, R; Han, J; Zhang, W.; et al. A perfect metamaterial polarization rotator. *Appl. Phys. Lett.* **2013**, *103*, 171107.

(15) Grady, N. K.; et al. Terahertz metamaterials for linear polarization conversion and anomalous refraction. *Science* **2013**, *340* (6138), 1304−1307.

(16) Cheng, Y.; et al. Dual-band and high-efficiency circular polarization convertor based on anisotropic metamaterial. *IEEE Access* **2020**, *8*, 7615−7621.

(17) Ding, X.; et al. Ultrathin Pancharatnam−Berry metasurface with maximal cross-polarization efficiency. *Adv. Mater.* **2015**, *27* (7), 1195−1200.

(18) Bai, J.; Yao, Y. Highly efficient anisotropic chiral plasmonic metamaterials for polarization conversion and detection. *ACS Nano* **2021**, *15* (9), 14263−14274.

(19) Mutlu, M.; et al. Asymmetric transmission of linearly polarized waves and polarization angle dependent wave rotation using a chiral metamaterial. *Optics Express* **2011**, *19* (15), 14290−14299.

(20) Zheng, Q.; Guo, C.; Ding, J. Wideband metasurface-based reflective polarization converter for linear-to-linear and linear-to-circular polarization conversion. *IEEE Antennas Wireless Propag. Lett.* **2018**, *17* (8), 1459−1463.

(21) Zhu, H. L.; et al. Linear-to-circular polarization conversion using metasurface. *IEEE Trans. Antennas Propag.* **2013**, *61* (9), 4615−4623.

(22) Xu, J.; et al. Ultra-broadband linear polarization converter based on anisotropic metasurface. *Optics Express* **2018**, *26* (20), 26235−26241.

(23) Yin, F.; et al. Multi-functional device: manipulating linear and circular-polarization conversion in a terahertz chiral metamaterial. *Optics Express* **2023**, *31* (17), 27171−27182.

(24) Kaschke, J.; et al. A helical metamaterial for broadband circular polarization conversion. *Adv. Opt. Mater.* **2015**, 3 (10), 1411−1417.

(25) Zhao, Y.; Belkin, M. A.; Alù, A. Twisted optical metamaterials for planarized ultrathin broadband circular polarizers. *Nat. Commun.* **2012**, 3 (1), 870.

(26) Balthasar Mueller, J. P.; Rubin, N. A.; Devlin, R. C.; Groever, B.; Capasso, F. Metasurface polarization optics: Independent phase control of arbitrary orthogonal states of polarization. *Phys. Rev. Lett.* **2017**, *118* (11), 113901.

(27) Dorrah, H.; Rubin, N. A.; Zaidi, A.; Tamagnone, M.; Capasso, F. Metasurface optics for on-demand polarization transformations along the optical path. *Nat. Photonics* **2021**, *15* (4), 287−296.

(28) Zaidi, U. N.; Rubin, N. A.; Dorrah, A. H.; Park, J.-S.; Capasso, F. Generalized polarization transformations with metasurfaces. *Opt. Express* **2021**, *29* (24), 39065−39078.

(29) Wang, S.; Deng, Z.L.; Wang, Y.; Zhou, Q.; Wang, X.; Cao, Y.; Guan, B.O.; Xiao, S.; Li, X. Arbitrary polarization conversion dichroism metasurfaces for all-in-one full Poincaré sphere polarizers. *Light: Sci. Appl.* **2021**, *10*, 24.

(30) Gou, Y.; Ma, H. F.; Wang, Z. X.; Wu, L. W.; Wu, R. Y.; Cui, T. J. Dual-band chiral metasurface for independent controls of spin-selective reflections. *Opt. Express* **2022**, *30* (8), 12775−12787.

(31) He, J.; et al. Alignment-Free Bilayer Moiré Metasurfaces with Tunable Twist Angles. *ACS Photonics* **2025**, *12* (8), 4608−4615.

(32) Liu, N.; et al. Stereometamaterials. *Nat. Photonics* **2009**, *3* (3), 157−162.

(33) Liu, M.; et al. Incident-angle-insensitive and polarization independent polarization rotator. *Optics Express* **2010**, *18* (11), 11990−12001.
(34) Wu, Z.; Ra'di, Y.; Grbic, A. Tunable metasurfaces: A polarization rotator design. *Phys. Rev. X* **2019**, *9* (1), 011036.
(35) Dicandia, F. A.; Genovesi, S. Design of a transmission-type polarization-insensitive and angularly stable polarization rotator by using characteristic modes theory. *IEEE Trans. Antennas Propag.* **2023**, *71* (2), 1602−1612.
(36) Liu, W.; Wang, S. R.; Dai, J. Y.; Zhang, L.; Chen, Q.; Cheng, Q.; Cui, T. J.; et al. Arbitrarily rotating polarization direction and manipulating phases in linear and nonlinear ways using programmable metasurface. *Light Sci Appl.* **2024**, *13* (1), 172.
(37) Cheng, G.; Si, L.; Tang, P.; et al. Study of symmetries of chiral metasurfaces for azimuth-rotation-independent cross polarization conversion. *Opt. Express* **2022**, *30* (4), 5722−5730.
(38) Wang, J.; Shen, Z.; Gao, X.; et al. Cavity-based linear polarizer immune to the polarization direction of an incident plane wave. *Opt. Lett.* **2016**, *41* (2), 424−427.
(39) Ivan, F.-C.; Fruhnert, M.; Rockstuhl, C. Objects of maximum electromagnetic chirality. *Phys. Rev. X* **2016**, *6* (3), 031013.
(40) Gorkunov, M. V.; Antonov, A. A.; Kivshar, Y. S. Metasurfaces with maximum chirality empowered by bound states in the continuum. *Phys. Rev. Lett.* **2020**, *125* (9), 093903.
(41) Hussain, S.; Liu, Q.; Maroof, Z.; et al. Ultra-broadband and high-efficiency planar chiral metamaterial. *Opt. Lett.* **2022**, *47* (21), 5700−5703.
(42) Wang, Z.; Jia, H.; Yao, K. W.; et al. Circular dichroism metamirrors with near-perfect extinction. *ACS Photonics* **2016**, *3* (11), 2096−2101.
(43) Menzel, C. H.; Rockstuhl, C.; et al. Asymmetric transmission of linearly polarized light at optical metamaterials. *Phys. Rev. Lett.* **2010**, *104* (25), 253902.
(44) Ye, Y.; He, S. 90° polarization rotator using a bilayered chiral metamaterial with giant optical activity. *Appl. Phys. Lett.* **2010**, *96* (20), 203501.
(45) Gansel, J. K.; Thiel, M.; Rill, M. S.; et al. Gold helix photonic metamaterial as broadband circular polarizer. *Science* **2009**, *325* (5947), 1513−1515.
(46) Yu, N.; Capasso, F. Flat optics with designer metasurfaces. *Nat. Mater.* **2014**, *13* (2), 139−150.
(47) Arbabi, Y. H.; Bagheri, M.; et al. Dielectric metasurfaces for complete control of phase and polarization with subwavelength spatial resolution and high transmission. *Nat. Nanotechnol.* **2015**, *10* (11), 937−943.
(48) Dorrah, H.; Park, J.-S.; Palmieri, A.; et al. Free-standing bilayer metasurfaces in the visible. *Nat. Commun.* **2025**, *16* (1), 3126.
(49) Li, Y.; Li, J.; Zhao, Y.; Gan, T.; Hu, J.; Jarrahi, M.; Ozcan, A.; et al. Universal Polarization Transformations: Spatial Programming of Polarization Scattering Matrices Using a Deep Learning-Designed Diffractive Polarization Transformer. *Adv. Mater.* **2023**, *35* (51), 2303395.
(50) Karim, A.; Martin, O. J. F. Fundamental properties and classification of polarization converting bianisotropic metasurfaces. *IEEE Trans. Antennas Propag.* **2021**, *69* (9), 5653−5663.
(51) Karim, A.; Tiukuvaara, V.; Martin, O. J. F. Spatial symmetries in nonlocal multipolar metasurfaces. *Adv. Photonics* **2023**, *5* (4), 046001−046001.
(52) Liu, M.; et al. Spontaneous chiral symmetry breaking in metamaterials. *Nat. Commun.* **2014**, *5* (1), 4441.
(53) Parvinnezhad Hokmabadi, M.; Philip, E.; Rivera, E.; Kung, P.; Kim, S.M. Plasmon-induced transparency by hybridizing concentric-twisted double split ring resonators. *Sci. Rep.* **2015**, *5* (1), 15735.
(54) Saleh, B. E. A.; Teich, M. C. *Fundamentals of Photonics*; 3rd ed.; Wiley, 2019.
(55) Zhu, Z.; Liu, H.; Jiang, Z.; Lv, T.; Guan, C.; Shi, J. Manipulating broadband polarization conversion in metamaterials. *J. Appl. Phys.* **2017**, *122* (21), 215101.
(56) Zhang, B.; Zhu, C.; Zhang, R.; Yang, X.; Wang, Y.; Liu, X. Ultra-broadband angular-stable reflective linear to cross polarization converter. *Electronics* **2022**, *11* (21), 3487.
(57) Rashid, A.; Murtaza, M.; Zaidi, S. A. A.; Zaki, H.; Tahir, F. A. A single-layer, wideband and angularly stable metasurface based polarization converter for linear-to-linear cross-polarization conversion. *PLoS One* **2023**, *18* (1), No. e0280469.
(58) Li, K.; Shen, C.; Chu, H.; Lai, Y. Angle-dependent multifunctional metasurfaces for wave diffusing under oblique incident angles. *Appl. Phys. Lett.* **2025**, *126*, 191705.

https://doi.org/10.1021/acsomega.5c11042
ACS Omega 2026, 11, 6264−6274